An Experimental and Computational Study on the Flow around a Hydrofoil with a Free-Surface

Wu-Joan Kim * and Suak-Ho Van †

Abstract

An experimental and computational study is carried out to investigate the flow characteristics around a hydrofoil when free surface presents. In the experimental study a NACA 0012 section is towed in a 2-D flume to document the wave profiles and surface pressure distribution. In the computational study a finite-difference scheme is employed to solve the Navier-Stokes equations and free surface profiles are obtained directly from the kinematic boundary condition. The calculated results are compared with those of the present and other two experiments to confirm the capability of the present method in free surface problems. The agreement between calculation and measurement is very good. It is found that the pressure on the upper(suction) side of the foil does not drop as much as in deeply submerged case and the lift deceases as a result.

1 Introduction

Hydrofoils have been widely used in modern ship-building engineering. High-speed vessels employ wing-like appendages to reduce the wetted surface areas and to control their postures. The flow around a hydrofoil is certainly influenced by the existence of free surface. However, the effect of free surface is not fully explored, although flow around a deeply submerged foil is readily understood.

There are some experiments which tried to investigate the effects of submergence on the lift of hydrofoils. Parkin et al.[1] and Duncan[2] measured the wave elevation and pressure distribution around a hydrofoil moving near the free surface. Some potential flow solutions are obtained by Bai[3, 4], who used a localized finite- ~ent method to calculate the wave elevation and pressure around a Joukowski foil. Shin[5, 6] calculated wave elevations generated by a NACA 0012 section and compared the results with Duncan's measurements. Although the effect of viscosity is included in his calculation, the Reynolds number is not high enough to simulate turbulent flows. Hino[7] solved the Navier-Stokes equations for low Reynolds number laminar flow, however the peak of pressure distribution is much less than that of the Euler solution. He also solved the Euler equations with unstructured grids[8] to study foil-wave interaction. Above two Navier-Stokes solutions, in general,

---

*Member, Korea Research Institute of Ships and Ocean Engineering
†Member, Korea Research Institute of Ships and Ocean Engineering

showed that the calculated wave amplitudes are less than those of the measurements. For the pressure distribution, especially on the suction side, the peak value is not reproduced well since flow turbulence is not considered in the calculation.

In the present paper, the experimental setup to measure the wave elevations and pressure distributions around a NACA 0012 wing section is described. Also the numerical method for the Reynolds-averaged Navier-Stokes equations, based on the finite-difference scheme in a collocated grid system, is presented. For the validation of the present method, numerical solutions are given for the same geometry and flow conditions of the present and two other experimental cases.

2 Experiments

2.1 Apparatus

All the measurements are carried out in the 2-D wave-making flume of KRISO. The flume is 60cm wide, 80cm deep, and 25m long. Two side walls are made of transparent acryl plate(0.8cm thick). A piston-type wave maker is installed at one end of the flume, while wave-absorbing chips are piled up at the other end. However, the wave maker is not used in the present study, because only the foil-generated wave is of present interest.

The channel has two parallel rails, on which a towing carriage is sitting. This electronically controlled carriage can run up to 1.2 m/sec. The speed of the carriage is calibrated by using a manual stop-watch and the estimated error of carriage speed is less than 0.5%. A clamping device and lateral traversing mechanism is installed to hold and tow a hydrofoil model. The flume has a water pump and plumbing system to circulate water in either direction. However, guide vanes are not installed yet, thus, the model is towed by a carriage rather than the water is circulated.

2.2 Hydrofoil model

The model with a NACA 0012 section is made of aluminum. It has a chord of 30cm and a maximum thickness of 3.6cm at 9cm from the nose. The foil has 24 taps on the upper surface and 23 taps on the lower surface to measure the surface pressure distribution. The span of the foil is 25cm. To ensure two-dimensionality of the flow, a false wall is installed at one edge of the foil, while the other edge had small gap with a side wall of the flume.

A vertical rod bolted at the fringe of the hydrofoil is clamped at the traversing mechanism of carriage to hold the foil and fringe/false wall. The false wall is 55cm deep and 150.5cm long (44.5cm upstream and 106cm downstream from the center of the foil) and a small tin plate is attached in front of false wall to minimize the influence of the false wall into the measurement region. It is, however, difficult to reduce the generation of Kelvin wave due to the false wall and the magnitude of which is more than 10% of foil-generated waves. Since separation of two components out of measured wave profiles is not so easy especially when wave breaking occurred and no correction is made.

2.3   Measurement

The height of hydrofoil-generated wave is measured using a capacitance-type wave-height gauge installed at 14.9cm inward from the side wall. A triggering switch is placed at a known position to find the position of the probe relative to the running hydrofoil. A post-filter/amplifier (Frequency Devices 9002) is used along with a wave monitor to increase the signal-to-noise ratio. The amplified voltage signal is digitized by A/D converter (MCLDAS) installed in PC 486. Surface pressure measurement is carried out using two Validyne pressure transducers (DP45-22), Carrier Demodulators (CD15), and two 24-channel Scanivalve systems controlled by a SCSP24 solenoid controller.

A Pitot tube is located upstream of the false wall on the other side of measurement region to monitor the speed of carriage. Since pressure transducers are differential type, the static pressure from the Pitot tube is used as a reference pressure. Diaphragms with the range of 14cm water head are used after the static calibration. To prevent air bubble from interfering the pressure measurement, boiled water is filled inside of the tubes and scanners from a reservoir. Since the foil rather than the water is moved, the pressure on only one tap can be measured during a run and 24 runs are required to complete one set of pressure measurements. For each run, data are collected during 3 seconds with the sampling rate of 50 Hz.
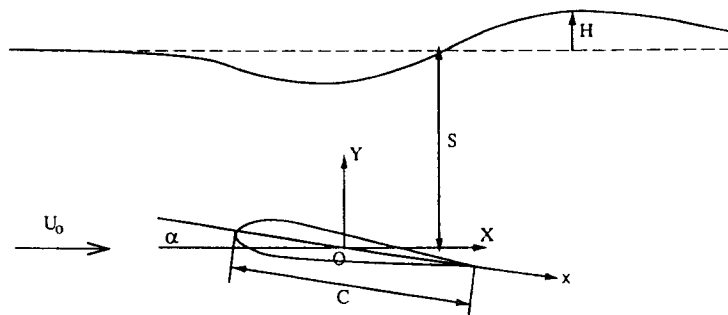

Figure 1 The coordinate sytem

3   Numerical methods

3.1   Governing equations

In the present study only two-dimensional problems are solved, but for generality, mathematical formulations are presented in three-dimensional curvilinear coordinates with tensor notations. The equations of fluid motion in Cartesian coordinates (x, y, z) for unsteady, three-dimensional turbulent flow of an incompressible fluid are considered. x denotes the inflow direction and y has the opposite direction to the gravitational acceleration as shown in figure 1. The Reynolds-averaged equations with an isotropic eddy viscosity model in non-dimensional form can be written in Cartesian tensor notation as follows.

Continuity equation

$$\frac{\partial u_k}{\partial x_k} = 0. \tag{1}$$

Momentum transport equations

$$\frac{\partial u_i}{\partial t} + u_j\frac{\partial u_i}{\partial x_j} = -\frac{\partial \hat{p}}{\partial x_i} + \frac{1}{R_{eff}}\nabla^2 u_i + \frac{\partial \nu_t}{\partial x_j}\left(\frac{\partial u_j}{\partial x_i} + \frac{\partial u_i}{\partial x_j}\right), \tag{2}$$

where $x_i = (x,y,z)$, $u_i = (u,v,w)$, $\frac{1}{R_{eff}} = \frac{1}{R_e} + \nu_t$ and $\hat{p} = p + \frac{y}{F_n^2} + \frac{2}{3}k$. The turbulent kinetic energy is included in the piezo-metric pressure, since the zero-equation turbulence model can not isolate k in the equation.

The summation convention is used, i.e., all the terms having repeated indices such as j and k of (1) and (2) should be summed. It should be noted that, for Cartesian tensors, there is no distinction between contravariant and covariant components. The equations are non-dimensionalized by a characteristic length L_o (chord length of foil section C in the present study), a reference velocity U_o (the velocity of uniform incoming flow), and the density of the fluid ρ. The Reynolds and Froude numbers are defined by $R_e = \frac{U_o L_o}{\nu}$ and $F_n = \frac{U_o}{\sqrt{gL_o}}$, respectively, where ν is the kinematic viscosity and g is the gravitational acceleration. The Baldwin-Lomax model[9] is employed for turbulence closure. The grid system is generated using Knight's method[10] and the details can be found in Kim[11].

With the body-fitted coordinate system determined, the transport equations in the physical domain (x,y,z) are transformed into those in the computational domain (ξ,η,ζ). The governing equations in generalized coordinates are given by

$$\frac{1}{J}\frac{\partial}{\partial \xi^m}(JU^m) = \frac{1}{J}\frac{\partial}{\partial \xi^m}(b_i^m u_i) = 0, \tag{3}$$

$$\frac{\partial u_i}{\partial t} + U^k\frac{\partial u_i}{\partial \xi^k} = -\frac{1}{J}b_i^k\frac{\partial \hat{p}}{\partial \xi^k} + \frac{1}{R_{eff}}\nabla^2 u_i + \left(\frac{1}{J}b_j^k\frac{\partial \nu_t}{\partial \xi^k}\right)\left[\left(\frac{1}{J}b_i^m\frac{\partial u_j}{\partial \xi^m}\right) + \left(\frac{1}{J}b_j^m\frac{\partial u_i}{\partial \xi^m}\right)\right], \tag{4}$$

where the contravariant velocity components are defined by $U^k = \frac{1}{J}b_j^k u_j$, and the definition of geometric coefficients can be found in Kim[11].

3.2 Discretization

In the finite-difference schemes the derivatives with respect to spatial and temporal variables are approximated using difference forms. It is easier to represent these difference forms as follows.

$$\delta_{\xi^k}^- = \frac{1}{6}\left[(\ )_{k-2} - 6(\ )_{k-1} + 3(\ )_k + 2(\ )_{k+1}\right] \text{ (3rd order backward-biased)}$$

$$\delta_{\xi^k}^+ = \frac{1}{6}\left[-2(\ )_{k-1} - 3(\ )_k + 6(\ )_{k+1} - (\ )_{k+2}\right] \text{ (3rd order forward-biased)}$$

$$\delta_{\xi^k} = \tfrac{1}{2}\left[-(\ )_{k-1} + (\ )_{k+1}\right] \text{ (2nd order central)}$$

$$\tilde{\delta}_{\xi^k} = \left[-(\ )_{k-\frac{1}{2}} + (\ )_{k+\frac{1}{2}}\right] \text{ (half-interval 2nd order central)}$$

The convection terms are discretized by using the so-called upwind scheme and the diffusion terms are central-differenced. The Euler-implicit method is applied for the time integration after local linearization of convection coefficients. The discretized momentum equations are

$$\frac{(u_i^{n+1}-u_i^n)}{\Delta t} + \tfrac{1}{2}\left(U^k + \mid U^k\mid\right)^n \delta_{\xi^k}^-(u_i^{n+1}) + \tfrac{1}{2}\left(U^k - \mid U^k\mid\right)^n \delta_{\xi^k}^+(u_i^{n+1}) =$$
$$-\tfrac{1}{J}b_i^k \delta_{\xi^k}(\hat{p}^{n+1}) + \tfrac{1}{R_{eff}}\left[g^{jj}\tilde{\delta}_{\xi^j}(\tilde{\delta}_{\xi^j}(u_i^{n+1})) + NO(u_i^n) + f^k\delta_{\xi^k}(u_i^{n+1})\right]$$
$$+ \left(\tfrac{1}{J}b_j^k \delta_{\xi^k}(\nu_t)\right)\left[\left(\tfrac{1}{J}b_i^m\delta_{\xi^m}(u_j^n)\right) + \left(\tfrac{1}{J}b_j^m\delta_{\xi^m}(u_i^n)\right)\right],$$

where

$$NO(u_i) = g^{jk}\delta_{\xi^j}(\delta_{\xi^k}(u_i))(j \neq k). \tag{5}$$

The superscripts $n, n+1$ represent the present and next time step, respectively. It should be noted that some of source terms are lagged. The discretized momentum transport equations (5) are solved by using a Peaceman- Rachford type ADI method. The implicit method in each direction results in the penta-diagonal matrices, for which a highly vectorized solver is available.

3.3 Pressure-velocity coupling

If pressure is known, equation (5) can be employed to solve equation (4) for (u, v, w). However, the pressure is not known a prior and must be determined by requiring the velocity field to satisfy the continuity equation (3). A MAC-type projection method is used to obtain pressure ensuring the divergence-free velocity field.

In the present study the collocated(non-staggered) grid system is used, where all the velocity components and pressure are defined at the same location. To avoid the oscillatory pressure field (checker-board problem), the fourth order dissipation is added in the pressure equation following Sotiropoulos et al.[12]. The details of pressure equation formulation and solution strategy can be found in Kim [11].

3.4 Boundary conditions

To solve the fully-elliptic momentum transport equations, it is necessary to specify the boundary conditions on all boundaries. The boundaries of physical domain consist of inlet, bottom surface, body boundary, exit and free surface. In the present study, two-block H-grid topology is adopted. The upper block includes the free surface boundary and the upper(suction) side of the foil section and the lower block includes the bottom boundary and the lower(pressure) side of the foil section. Along the block interface four grid points(two points from each side of the block) are overlapped to ensure the continuous change of flow variables across the block interface.

No-slip condition is directly applied to the foil surface since the Baldwin-Lomax turbulence model is valid through the near-wall sublayer. For the bottom surface, the symmetry condition is applied to simulate the restricted water channel in the experiment without resolving the boundary layer of the bottom surface. The inlet has uniform flow coming into the domain and the downstream velocities are extrapolated at exit.

Free surface profile is obtained directly from the kinematic free surface condition at each time step and the new profile is used to reconstruct grids in the upper block. Simple linear interpolation in the vertical direction is used. In principle, the so-called grid velocity should be considered when the grid system is moving with respect to the reference frame. However, since only the steady state solution is of interest, the grid velocity is not included in the formulation. In two-dimensional wave problem, the downstream or far field condition is of concern since reflection of the generated wave ruins the interior solution. A damping function is introduced in the kinematic free surface condition to reduce the effect of the downstream flow following Hino[8].

The kinematic free surface boundary condition without any approximation is

$$\frac{D(h(x,t)-y)}{Dt} = \frac{\partial h}{\partial t} + u\frac{\partial h}{\partial x} - v = 0 \quad \text{at} \quad y = h(x,t),$$

If an artificial damping $\gamma(x)$ is added, the above equation becomes

$$\left(\frac{h^{n+1} - h^n}{\Delta t}\right) + u^{n+1}\left(\frac{\partial h}{\partial x}\right)^{n+1} - v^{n+1} + \gamma(x) = 0 \quad \text{at} \quad y = h^n(x), \quad (6)$$

where $\gamma(x) = \Omega \left(\frac{x-x_d}{x_o-x_d}\right)^2 h(x)$ for $x_d \leq x \leq x_o$ and $\gamma(x) = 0$, otherwise. $x_d = x_o - 2\pi F_n^2$ and x_o is the location of exit boundary. It should be noticed that $2\pi F_n^2$ corresponds approximately to one wave length. It has been observed that if the damping is not added, the mean line of generated waves is oscillating.

The convection term of the kinematic free surface boundary condition $\left(\frac{\partial h}{\partial x}\right)^{n+1}$ is approximated by using a quadratic equation in the upstream direction (i.e., the 2nd order upwind scheme for non-uniform spacing). The 2nd order central difference scheme is also tested along with various values of Ω. The results from the central-difference scheme do not show any noticeable difference with those of the upwind scheme. Thus, in the present study, the quadratic interpolation in the upwind direction with Ω of 10 is used. It should be noted again that the grid system of the upper block is generated each time step to conform the free surface profile, thus the final grid system of a converged solution will provide the free surface elevation $h(x)$. However, it is not possible to take care of wave-breaking cases with this formulation, as most of free-surface conforming techniques are not appropriate to solve the free surface problem with wave breaking.

The dynamic free surface condition states that the stress components(one normal and two tangential components) are continuous across the free surface. The existence of boundary layer very near the free surface is neglected. Velocity components are extrapolated using interior values, while the piezo-metric pressure at the free surface is given by

$$\hat{p}^{n+1} = \frac{h^{n+1}}{Fn^2} \quad \text{at} \quad y = h^{n+1}. \quad (7)$$

4 Results and discussion

The numerical methods are applied to simulate the results of three experimental cases. The first one is the measurement described in the previous section, hereafter called KRISO case, and the second one is the measurements of Duncan[2]. He measured only wave profiles generated by a NACA 0012 section at the Froude number of 0.567. The last one is Parkin's[1] case in which the pressure distribution on the suction side of a 12% thick Joukowski foil section is measured in a water channel for $F_n = 0.95$. In the sequel, computed results are shown and compared with experimental data.
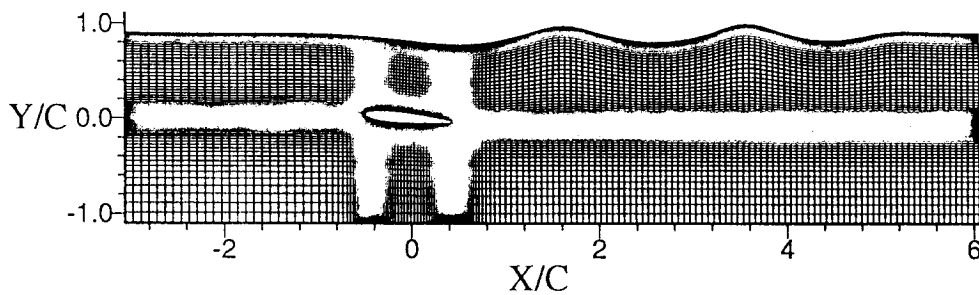
Figure 2 Generated grid system after convergence

4.1 KRISO case

As described in the section 2, a NACA 0012 foil section is towed at the water depth of $2C$ at Froude number of 0.567. In the calculation the solution domain consists of $-3C < X < 6C$ and $(S - 2C) < Y < S$, where S represents the depth of submergence of the mid-chord point of foil from the calm water surface and C is the chord length. 205 grids are distributed along the streamwise direction with 60 points over a foil surface, while 100 grids are used for upper and lower block (50 points each) of the solution domain. The Reynolds number of the experiment is 0.29×10^6, so is in the calculation. Figure 2 shows a typical grid system after convergence. Grid distribution is clustered near the foil section and the free surface in the vertical direction and at the leading and trailing edge in the horizontal direction. The block interface of solution domain consists of a horizontal line in front of the leading edge, after the trailing edge and the upper or lower surface of the foil.

The calculated wave profiles are compared with measured ones in figure 3. When the angle of attack is zero, wave breaking is observed for $S/C = 0.2$, and this case is not included in calculation. There are some differences in phases of waves, but wave heights show a reasonable agreements. When the angle of attack is 5°, wave breaking is observed for $S/C = 0.8$, thus, for one of the calculated cases($S/C = 0.5$), wave breaking appears as a sudden explosion of pressure value at the free surface. In figure 3 the solution just before the sudden divergence is shown since little attention is paid to the calculation of wave breaking. A huge crest near the trailing edge of the foil for $S/C = 0.5$ evidences wave-breaking phenomenon, while the calculated wave profile of $S/C = 0.9$ shows a phase lead, similarly to the case of angle of attack 0°. Pressure contours of four calculated cases are shown in figure 4. As mentioned earlier, the kinematic free surface condition applied

to the present calculation has a damping zone of one wave-length $(= 2\pi F_n^2)$ near the exit of the solution domain and wave height as well as pressure contours are damped out in the damping zone. However, this damping does not affect the interior solution ahead of the damping zone.
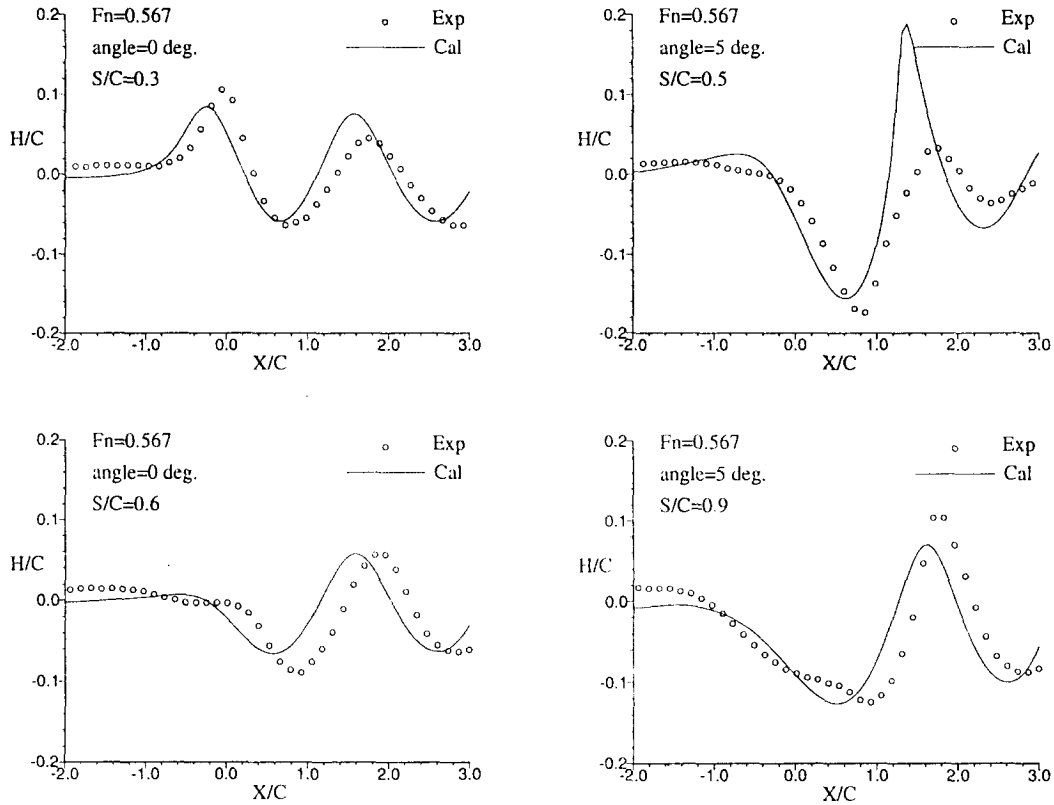

Figure 3 Comparison of wave profiles (KRISO case, $F_n = 0.567$)

Pressure contours near the upper(suction) side of the foil for $S/C = 0.3$ is much different from those for $S/C = 0.6$, showing the influence of free surface on the pressure distribution (i.e. lift and drag) over a foil surface. The same trend is obtained when the angle of attack is 5° as shown in figure 5. For $S/C = 0.5$, the solution breaks down before the wave system develops and very stiff change of pressure contours is observed near the first crest of the wave. The periodicity of the flow field expected in two-dimensional wave problems is well reproduced except the case with wave breaking. Pressure coefficients $C_p(= \frac{p}{\frac{1}{2}\rho U_o^2})$ along the foil surface is shown in figure 5 and compared with experimental data. Considering the results in figure 3, pressure distributions are expected to show discrepancies, however, the overall performance is reasonably good and the difference of pressure coefficients between the upper and lower side of the foil is almost the same.
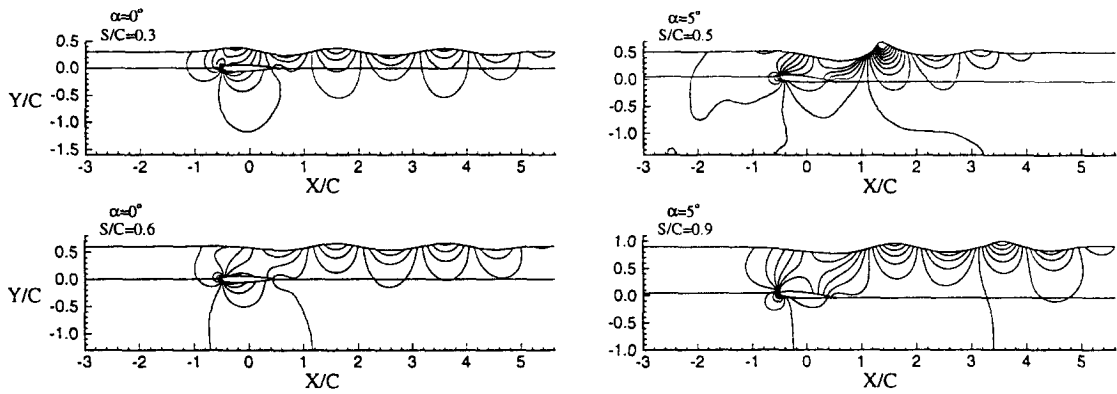
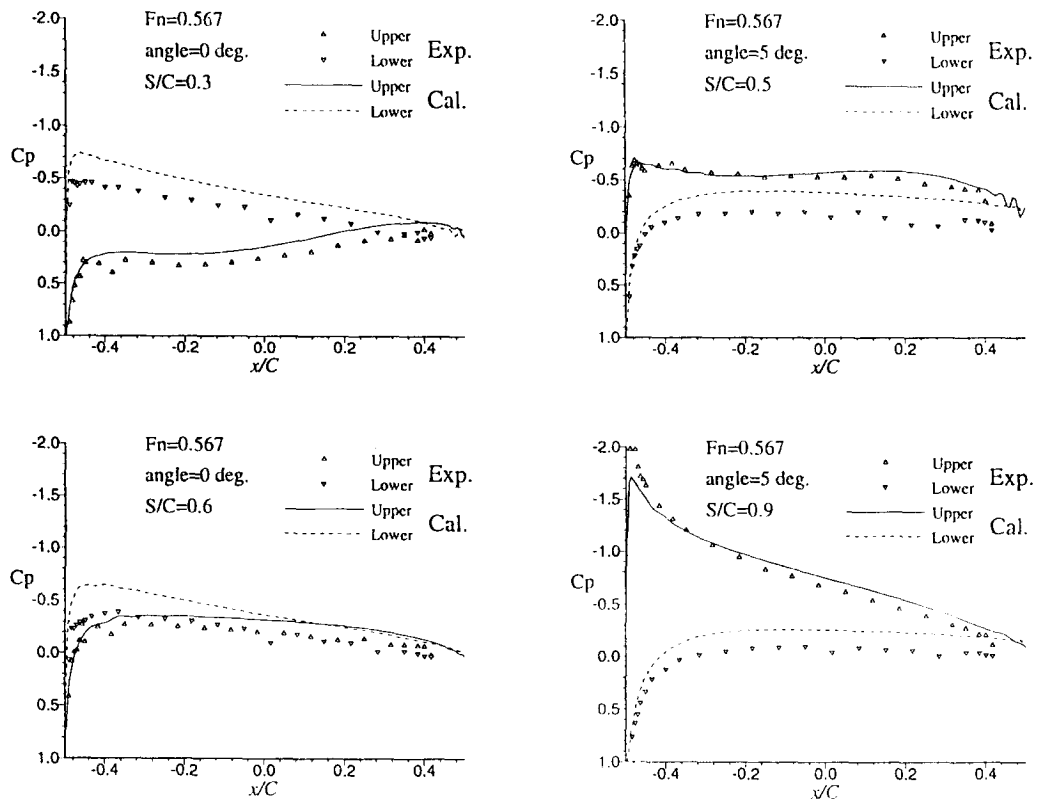Figure 4 Calculated pressure contours (KRISO case, $F_n = 0.567$)

Figure 5 Comparison of surface pressure distribution (KRISO case, $F_n = 0.567$)

4.2 Duncan's case

A NACA 0012 section with the chord length of 20.3cm is towed at the angle of attack of $5°$ in Duncan's experiment. He measured wave profiles for $S/C = 0.7833 \sim 1.2857$

generated by a foil section running at the Froude number of 0.567 and the Reynolds number of 0.142×10^6. His foil is placed at 0.8621C from the bottom of water tank where rope/pulley system pulled the foil section without interfering the free surface. Thus, his measurement is very reliable, even though the closeness of bottom would certainly affect the wave profiles. Unfortunately, he did not measure the pressure distribution over the foil surface.

For the computation, 225 grids are distributed for $-5C < X < 8C$ in streamwise direction and 100 grids are distributed vertically for $-0.8621C < Y < S$. Calculated wave profiles for 4 different depths are compared with Duncan's measurements in figure 6. Duncan found that wave breaking does not occur for $S/C = 0.9507$, however, it occurs if small disturbance is applied to the upstream of the foil. Duncan provided two different wave profiles for $S/C = 0.9507$, one set for non-breaking case and the other for breaking case due to small disturbance. Only the non-breaking case is compared in figure 6.

The agreement between calculation and measurement is very good for all four cases. The wave peaks in the calculation are predicted slightly lower than those of experiment. The calculated phases show good agreements with measurement,however, the agreements become less impressive as the wave height increases. Pressure contours are shown in figure 7. As depth of submergence decreases, the slope of pressure contours becomes severe since wave elevation increases.
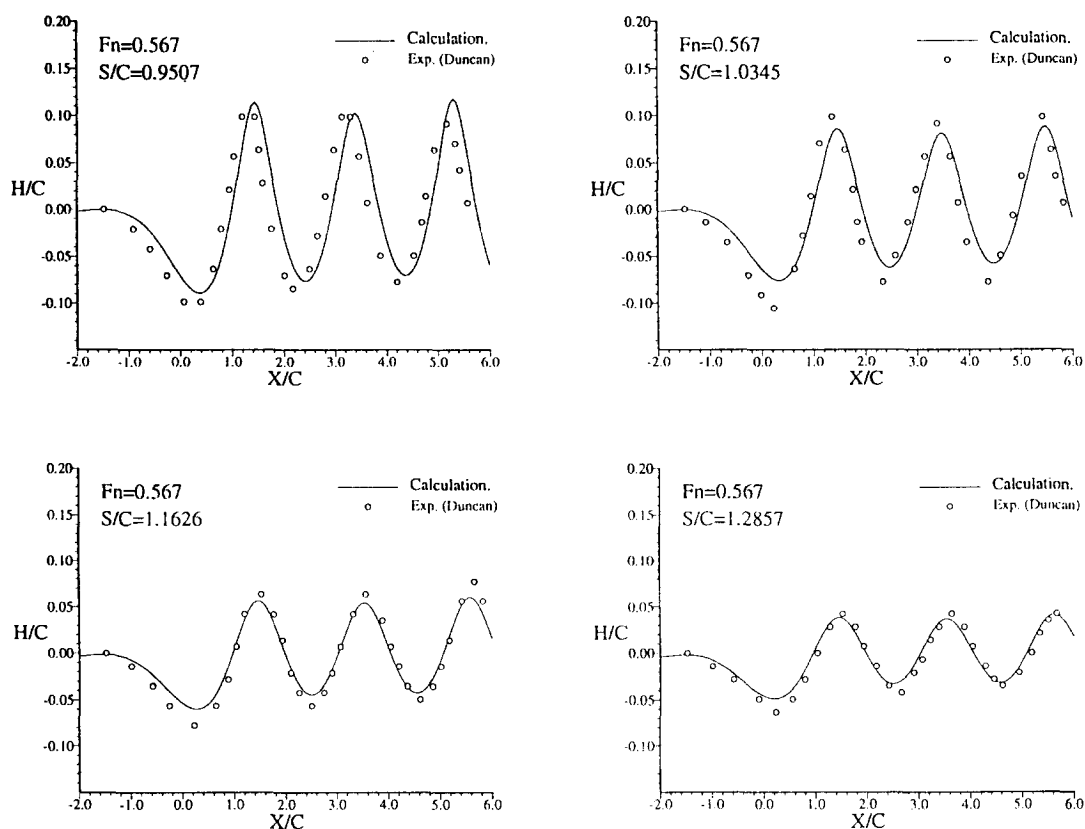

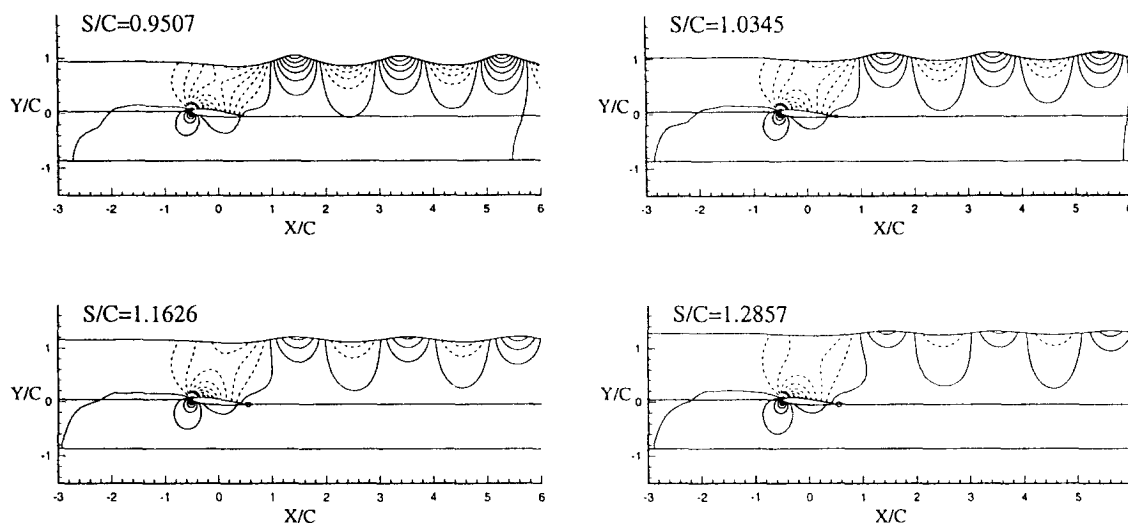Figure 6 Comparison of wave profiles (Duncan's case. $F_n = 0.567$)

Figure 7 Calculated pressure contours (Duncan's case, $F_n = 0.567$)

4.3 Parkin's case

Parkin[1] measured the pressure distribution on the suction(upper) side of a 12% thickness Joukowski foil at the angle of attack of $5°$ in a circulating water channel. The foil section used in the Parkin's experiment is not much different from the NACA 0012 sections used in Duncan and KRISO's experiment, but the Froude number range considered in Parkin's measurement is much broader than other experiments. For the present comparison, the Froude number of 0.95 is chosen since it has various depths of submergence and is far from the Froude number of the previous calculations and the resulting Reynolds number is 0.239×10^6.

The solution domain is increased three times in the streamwise direction since the wave length becomes three times longer than that of the previous cases. Because the depth of water channel is not clearly stated in the Parkin's paper, the bottom surface is assumed to be located $6C$ below the free surface in the present calculation. 225×100 grids are distributed in $-4C < X < 17C$ and $S - 6C < Y < S$. In figure 8, wave profiles calculated for six different depths of submergence are presented. It is surprising that wave elevation does not increase with the decrease of S/C when S/C is less than 0.5. It should be noticed that a crest-like hump appears first for $S/C = 0.4564$ and wave height decreases as the hump over the foil developed. Experimental data for wave elevations are not available.

Surface pressure distributions are compared in figure 9. At the deepest position $S/C = 1.7564$, pressure curve does not show any significant influence of free surface, however, as the foil approaches the free surface, the upper(suction) side is strongly affected by the existence of free surface. The prominent phenomenon is that the suction side pressure does not drop so much as in deep water, which results in severe decrease of the lift force. It is confirmed again that the existence of free surface decreases the lift, at least for Froude numbers of 0.567 and 0.95. The calculate results agree very well with Parkin's measurements, showing the capability of the numerical methods employed in the present

study. Pressure contours are shown in figure 10. The wave length is about $5.7C$ and the periodicity of the flow is represented very well.
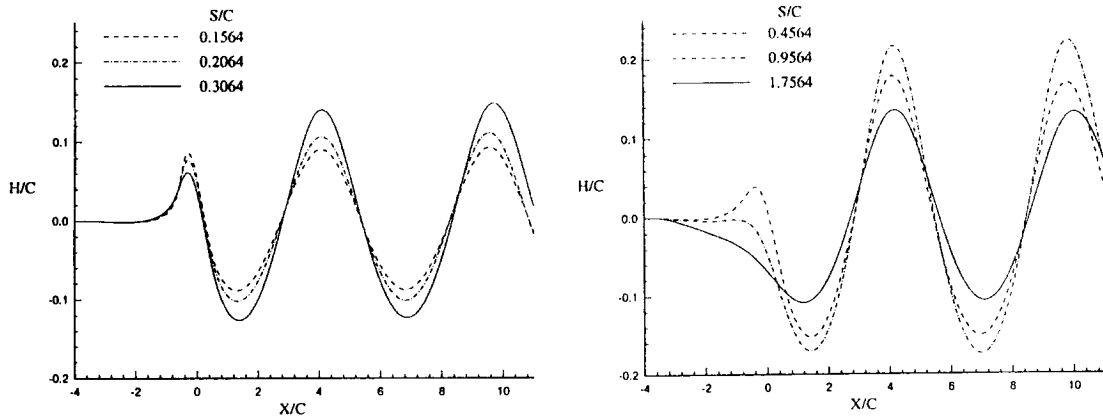

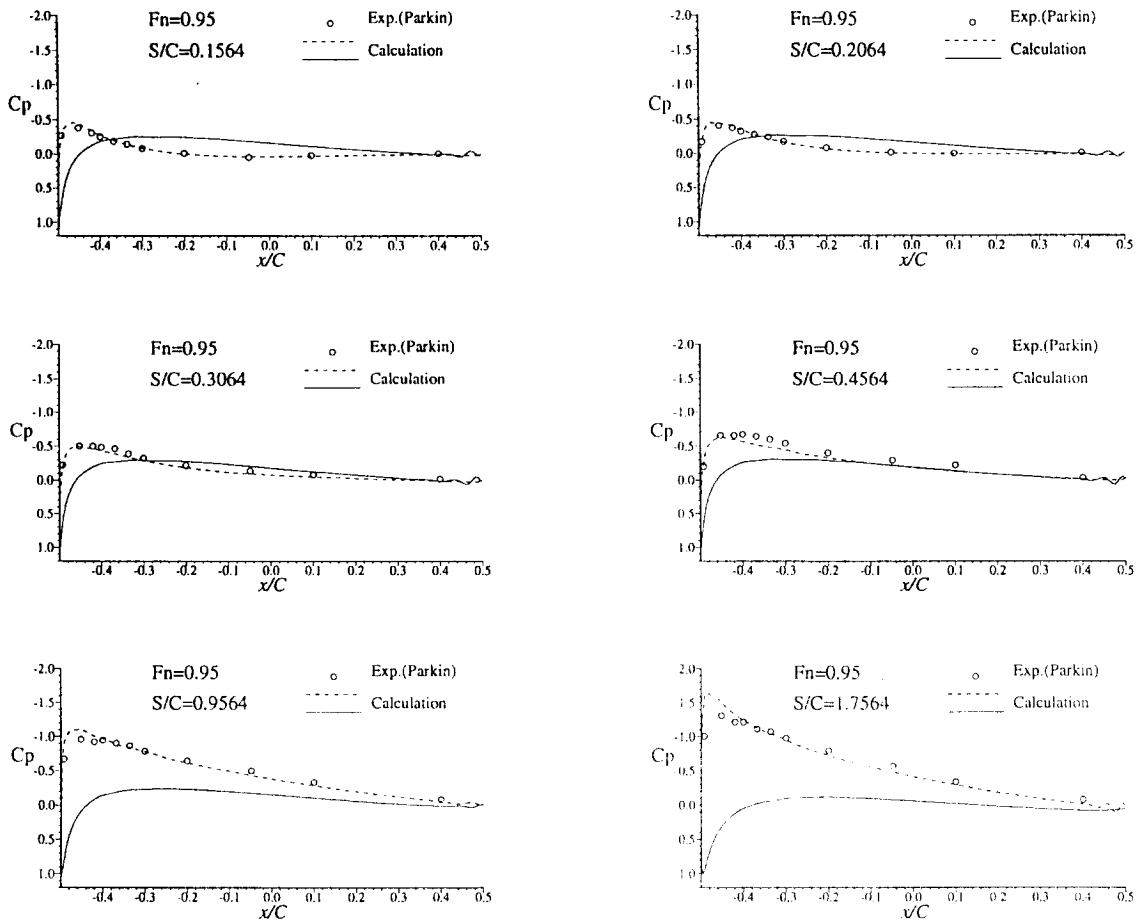Figure 8 Calculated wave profiles (Parkin's case, $F_n = 0.95$)

Figure 9 Comparison of surface pressure distribution (Parkin's case, $F_n = 0.95$)
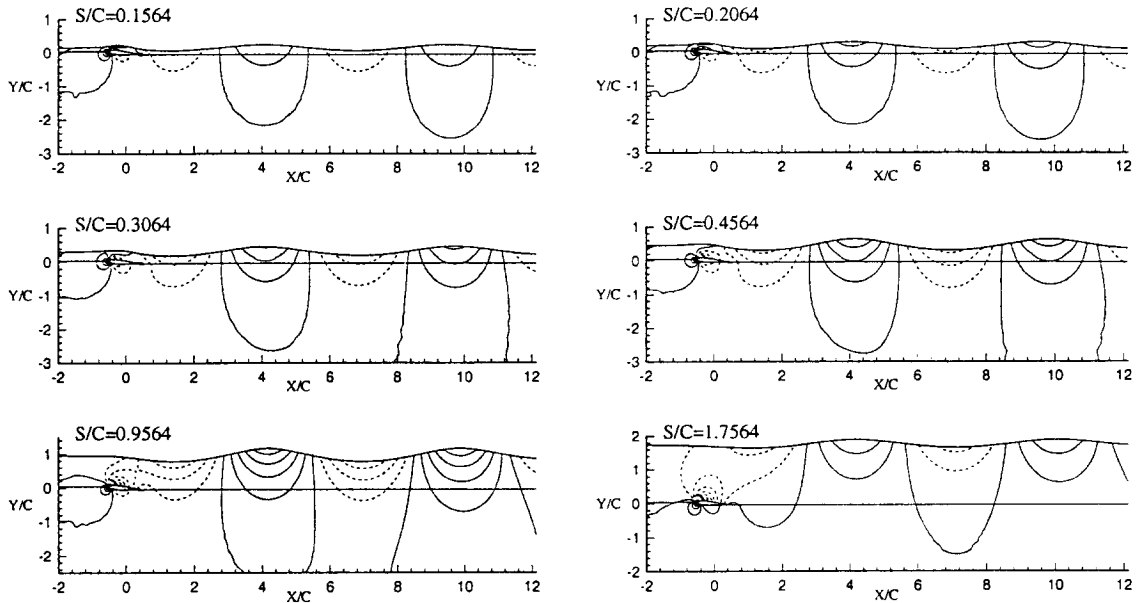
Figure 10 Calculated pressure contours (Parkin's case, $F_n = 0.95$)

5 Summary and recommendation

The effect of free surface on the pressure distribution of the hydrofoil running under the free surface is investigated by experiment and computation. Wave elevations and pressure distributions around the NACA 0012 section are measured in the 2-D flume of KRISO. A numerical method for the solution of two-dimensional Reynolds-averaged Navier-Stokes equations with free surface is developed. The collocated (non-staggered) grid system is employed along with the finite-difference (the 3rd order upwind-biased scheme) discretization. The grid system conformed the free surface profile at each time step, however, grid velocities are not considered, since only the steady state is of interest. The calculated results are compared with those of three experiments to confirm the capability of treating the free surface problems. The agreements between calculations and measurements are very good. It is found that the pressure on the suction(upper) side of the foil is influenced severely and the resulting lift decreases mainly because the suction side pressure does not drop as much as in deeply submerged case.

The present calculation is performed in two-block H-grid topology. It is well known that the C-type grid topology is more appropriate to resolve the flow around a foil but it is more difficult to solve the free surface problem in C-type grid system. However, when H-type grid is applied, the pressure drop of the suction side near the leading edge is usually under-predicted. It is very hard to satisfy the conformity of grids for both free-surface and foil surface. These difficulties can be avoided if more flexible, geometry-adapting grid system is used, such as a patched grid system or a composite(over-laid) grid system.

Acknowledgement

References

[1]   Parkin, B.R., Perry, B. and Wu, T.Y. (1956), "Pressure Distribution of a Hydrofoil near the Water Surface," *Journal of Applied Physics,* Vol. 27, No. 3, pp. 232-241.

[2]   Duncan, J.H. (1983), "The Breaking and Non-breaking Wave Resistance of a Two-Dimensional Hydrofoil," *Journal of Fluid Mechanics,* Vol. 126, pp. 507-520.

[3]   Bai, K.J. (1978), "A Localized Finite-Element Method for Two-Dimensional Steady Potential Flows with a Free Surface," *Journal of Ship Research,* Vol. 22, No. 4, pp. 216-230.

[4]   Bai, K.J. and Han, J.H. (1994), "A Localized Finite-Element Method for the Nonlinear Steady Waves Due to Two-Dimensional Hydrofoil," *Journal of Ship Research,* Vol. 38, No. 1, pp. 42-51.

[5]   Shin, M.S. and Mori, K-H (1989), "Numerical Computation of 2-Dimensional Waves Behind a Hydrofoil," *Journal of The Society of Naval Architects of Japan,* Vol. 163, pp.17-22.

[6]   Shin, M.S. and Mori, K-H (1989), "On Turbulent Characteristics and Numerical Simulation of 2-Dimensional Sub-breaking Waves," *Journal of The Society of Naval Architects of Japan,* Vol. 165, pp.1-7.

[7]   Hino, T. (1989), "Numerical Computation of a Free Surface Flow Around a Submerged Hydrofoil by the Euler/Navier-Stokes Equations," *Journal of The Society of Naval Architecture of Japan,* Vol. 164, pp. 9-17.

[8]   Hino, T. (1993), "A Finite-Volume Method with Unstructured Grid for Free Surface Flow Simulations," *Proceedings of 6th International Conference on Numerical Ship Hydrodynamics,* August 2-5, Iowa City, IA.

[9]   Baldwin, B.S., Lomax, H., "Thin Layer Approximation and Algebraic Model for Separated Turbulent Flows," *AIAA Paper,* 78-257.

[10] Visbal, M., Knight, D. (1982), "Generation of Orthogonal and Nearly Orthogonal Coordinates with Grid Control near Boundaries," *AIAA Journal,* Vol. 20, No. 3.

[11] Kim, W.J. (1994), "An Experimental and Computation Study on the Pressure Distribution Around a Hydrofoil Moving Under the Free Surface," Report UCE554-1845D, KRISO, Korea.

[12] Sotiropoulos, F., Kim, W.J., Patel V.C. (1994), "A Computational Comparison of Two Incompressible Navier-Stokes Solvers in Three-dimensional Laminar Flows," *Computers and Fluids,* Vol. 23, No. 4, pp.627-646.